

Effective Ion Mobility and Long-Term Dark Current of Metal Halide Perovskites with Different Crystallinities and Compositions

Marisé García-Batlle, Sarah Deumel, Judith E. Huerdler, Sandro F. Tedde, Osbel Almora, and Germà Garcia-Belmonte*

Ion transport properties in metal halide perovskite still constitute a subject of intense research because of the evident connection between mobile defects and device performance and operation degradation. In the case of X-ray detectors, dark current level and instability are regarded to be connected to the ion migration upon bias application. Two compositions (MAPbBr₃ and MAPbI₃) and structures (single- and microcrystalline) are checked by the analysis of long-term dark current evolution. Electronic current increases with time before reaching a steady-state value within a response time (from 10⁴ down to 10 s) that strongly depends on the applied bias. A coupling between electronic transport and ion kinetics exists that ultimately establishes the time scale of electronic current. Effective ion mobility μ_i is extracted for a range of applied electric field ξ . While ion mobility results field-independent in the case of MAPbI₃, a clear field enhancement is observed for MAPbBr₃ ($\partial\mu_i/\partial\xi > 0$), irrespective of the crystallinity. Both perovskite compounds present effective ion mobility in the range of $\mu_i \approx 10^{-7}$ – 10^{-6} cm² V⁻¹ s⁻¹, in accordance with previous analyses. The ξ -dependence of the ion mobility is related to the lower ionic concentration of the bromide compound. Slower migrating defect drift is suppressed in the case of MAPbBr₃, in opposition to that observed here for MAPbI₃.

1. Introduction

Perovskites have been explored in almost all fields of material science.^[1,2] Considerable efforts have been made on examining the causes of hysteresis in the current–voltage curves,^[3–5] the nature of charge traps, defects,^[6,7] grain boundaries,^[8] origins of ion migration,^[9–11] not only in the field of solar cells and light emitters devices,^[12] but also as key materials in fuel cells^[13] and electrodes for water electrolyzers.^[14] By tailoring the composition of the perovskite compounds, a variety of physical properties appears, such as ferroelectric,^[15] dielectric, piezoelectric, magnetic,^[16] catalytic,^[17] photovoltaic, electronic-ionic-conduction,^[18] and superconducting properties.^[19]


Recently, metal halide perovskite (HP) materials have been successfully used in X-ray imaging and ionizing radiation detectors.^[20,21] The chemical formula APbX₃ (where A is a cation and X is the halide anion) comprises reasonably high Z elements, which are helpful to stop

high-energy radiation photons. HPs exhibit the so-called defect tolerance which is connected to the transport properties allowing to maximize the product of the charge mobility and carrier lifetime by minimizing the bulk/surface defect density.^[22–24] Furthermore, direct semiconductor radiation detectors based on Pb-HPs can be grown and processed in solution at relatively low temperatures and from low-cost basic raw materials.^[25,26]

Fast and efficient detection of hard X- and γ -ray with high energy resolution is critical for medical and industrial applications.^[27] The direct conversion X-ray detectors transform the incident X-ray photons directly into electrical signals, and present an advantage in terms of high spatial resolution in comparison to indirect detectors such as CsI.^[28] Besides optimization in material composition and device architecture, the conventional direct detectors, such as amorphous selenium (α -Se),^[29] suffer from their low mobility-lifetime ($\mu\tau$) product and small atomic number which limit their sensitivity.^[24,30] In contrast, HPs exhibit large $\mu\tau$ -product and strong stopping power. However, the persistent drawback of ion migration results in deleterious and unstable dark current.^[31–33] In fact, induced dark current and also

M. García-Batlle, O. Almora, G. Garcia-Belmonte
Institute of Advanced Materials (INAM)
Universitat Jaume I
12006 Castelló, Spain
E-mail: garciag@uji.es

S. Deumel, J. E. Huerdler, S. F. Tedde
Siemens Healthineers AG
Technology Excellence
Guenther-Scharowsky-Strasse 1, 91058 Erlangen, Germany

 The ORCID identification number(s) for the author(s) of this article can be found under <https://doi.org/10.1002/adpr.202200136>.

© 2022 The Authors. Advanced Photonics Research published by Wiley-VCH GmbH. This is an open access article under the terms of the Creative Commons Attribution License, which permits use, distribution and reproduction in any medium, provided the original work is properly cited.

DOI: 10.1002/adpr.202200136

photocurrent drift under a large electric field negatively alter the intrinsically good performance of X-ray detectors.^[34]

Significant progress has been reported in substrates, selective electrodes, and stable sensing layers for accurate detection. Highly sensitive active nanolayers have been tested for gas-based detectors to increase the long-term current stability.^[35] The use of noble metals such as Pd and Pt on the host materials has been examined for sensitivity improvement.^[36] Other strategies for sensing performances are based on controlling the defect chemistry, from ion-doping/loading techniques^[37] for stability enhancement^[38] to atomistic surface passivation to heal the surface defects,^[39,40] and also introducing charge transport layers at the outer interfaces,^[34] which may, potentially, inhibit the ion migration. However, dark current has been reported in perovskite-based detectors, with values larger than those registered with commercial devices,^[29,30] over which the photocurrent should be detected. Moreover, such a dark current under continuous biasing exhibits instability, which is detrimental to the transient response of the X-ray detectors.^[34] Ultimately, dark current values are too large to achieve high-quality images, with high resolution and contrast for accurate diagnosis.^[41] Therefore, it is essential to obtain high dark resistivity through further progress in material composition engineering and device architecture. Also crucial is to achieve a deep understanding on how ion migration governs the electronic current for the long-term operational stability of the detector.^[42,43]

In this work, chronoamperometry experiments are performed to study the long-term current transient response of different compositions of single-crystal (SC) and microcrystalline (MC) perovskite samples of MAPbBr₃ and MAPbI₃ at room temperature. Dissimilar current responses are encountered for the bromide-based perovskite samples and the iodine ones. Our findings corroborate the existence of a coupling between electronic transport and ion kinetics that ultimately establishes the time scale of electronic dark current.^[10] In all cases, electronic current increases with time before reaching a steady-state value within a response time (from 10⁴ down to 10 s) that strongly depends on the applied bias. We highlight that fitting the long-term dark current transient curve provides an estimation of the intrinsic parameters such as the ionic mobility which is in the range of $\mu_i \approx 10^{-7}$ – 10^{-6} cm² V⁻¹ s⁻¹ for the studied samples.

2. Results and Discussion

MAPbBr₃-SC of ≈ 2 mm thick symmetrically face-to-face contacted with Cr electrodes and MC samples of ≈ 1 mm thick of MAPbX₃ (X : Br⁻, I⁻) asymmetrically contacted with Pt and Cr electrodes were investigated in the dark by registering the long-term current transient response after voltage biasing, as shown in Figure 1. The transients were measured by following a previously used protocol,^[10] by application of a forward bias for SC, symmetrically contacted samples, and a reverse bias (Pt positively and Cr negatively contacted) for MC samples, followed by a zero-bias equilibration period (see Figure S1, Supporting Information) of ≈ 3000 s. In Figure S2, Supporting Information, the used biasing protocol for each sample is shown, which exhibits sufficient reproducibility. An increasing trend in

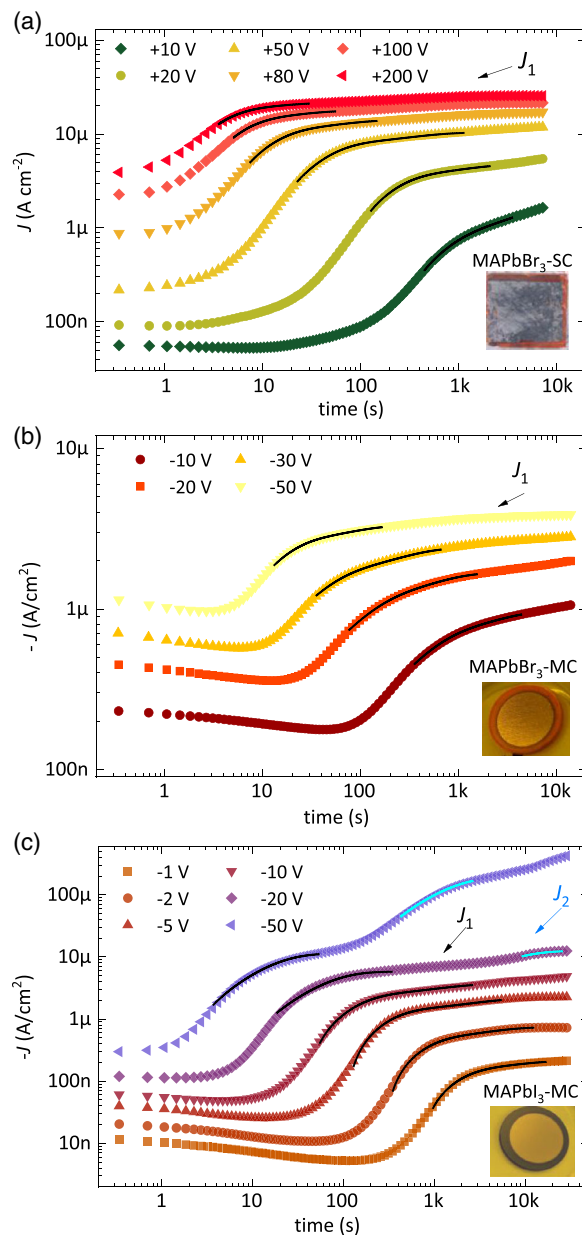


Figure 1. Long-term current response upon a biasing protocol for: a) ≈ 2 mm thick MAPbBr₃-SC, b) ≈ 1.5 mm thick MAPbBr₃-microcrystalline (MC), c) ≈ 1 mm thick MAPbI₃-MC. Note the experimental current transient with the corresponding fittings (black solid lines) for each curve following Equation (1). The parameters J_1 and J_2 correspond to the steady-state current during the first and second exponential rise respectively. After each bias, the device is kept under short-circuit (0-V bias) conditions to observe the relaxation current. See the long-term current response of each sample for the other two cycles in Figure S3–S5, respectively. In the inset is shown the top-view image of each sample. Data in (a) reproduced under the terms of the CC-BY license.^[10] Copyright 2022, The Authors. Published by American Chemical Society.

the current transient can be seen (Figure 1), although some particularities were observed, at different time scales, depending on the sample composition and crystallinity.

By first examining the global transient response of a MAPbBr₃-SC (Figure 1a) under continuous application of forward bias, the current increases from a rather constant value at shorter times ($t < 1$ –10 s), that finally saturates approaching steady-state values J_1 at longer times. This behavior has been noticed previously in MAPbBr₃ single-crystal samples^[10] and agrees with the evidence that the higher the bias the faster the current increase. In Figure 1b, an additional feature appears during the transient of a MAPbBr₃-MC sample under reverse bias. At the beginning of the transient for $t < 5$ –50 s, a slight decrease of the current is observed, while for $t > 100$ s an exponential growth can be identified, as in the case of SC, that finally reaches a current steady state J_1 . As observed, the initial decrease represents a minor feature of the overall current evolution.

Figure 1c displays the more complex current transient response of a MAPbI₃-MC sample. Once more, for shorter times ($t < 50$ s) initial current tend to slightly decrease. Afterward, the current grows and seems to saturate at J_1 . This is consistent with previous observations in Figure 1a,b registered for Br-based perovskite samples at that polarization times. Interesting, the transient response of MAPbI₃-MC is different for bias lower than -10 V: a second current increase appears, which tends to a larger saturation value J_2 at longer times.

Then, the magnitude of the electronic current J , both for the first and second current increase, can be described as a function of the time constant τ of the ion migration process (see below) as

$$J = J_i(1 - e^{-t/\tau_i}) \quad (1)$$

being J_i and τ_i ($i = 1, 2$) the corresponding saturation current and response time for each current increase step. The fitting of Equation (1) to the current rise is plot in each transient as a solid line in Figure 1. As noted previously, the time constants reveal the dynamics of the ionic transport within the device,^[44] and can be assimilated to a drift-induced ionic time-of flight that effectively controls the time scale of the electronic current transient toward saturation, while the amplitude of the current response is determined by the electronic carriers (electrons and holes).^[10] It is also noticeable that inverted hysteretic responses are observed in Figure S6, Supporting Information,^[45–47] which correlate to the increment of the current over time reported here and inductive behaviors in the frequency domain.^[47]

Following the insights from our recent paper,^[10] we are able to rationalize the current phenomenology by assuming that the measured current is always an electronic current. However, a coupling between ionic and electronic currents exists in such a way that the slower species (ions) condition the value of the measured current, which actually monitors the faster carriers (electrons/holes). As ions move by the effect of the electric field (and eventually accumulate in the vicinity of the contacts), the kinetics of the electronic response follows the slow ion rearrangement. Whatever the ionic/electronic interplay mechanism is behind the current transients, it is evident that the initial homogeneous distribution of ions at zero bias hinders the charge extraction at short times, while the applied bias favors the electronic current flowing at longer times. The latter effect can be possibly due to: 1) an increment of the effective electronic doping in the bulk perovskite via field ionization; 2) a local increment

of effective doping caused by ion redistribution (dynamic doping).^[48] These two mechanisms would imply an increment in electronic conductivity (and consequently current) over time after bias application;^[49,50] Finally, 3) a reduction of contact electronic barriers via electrode polarization caused by ion accumulation, fostering as a consequence carrier injection or iv) a combination of all these effects may also occur. Elucidation of the effective mechanism occurring in perovskite-based devices needs an exhaustive analysis of different structures (electrodes, active material, buffer layers...) aimed at creating a coherent picture.

Now let us consider the behavior of the steady-state electronic current. From the long-current transients of Figure 1, one can obtain the J_1 - V curve in Figure 2 using the steady-state values of the first current step. The current value J_1 has been marked in Figure 1 for the three samples presented. From an allometric fit with a power law of the type $J_1 \propto V^\beta$, the extracted power β attains values between 0.98 and 1.05 with an average variability of ± 0.07 , which suggests an apparent ohmic conductivity regime for electronic charge carriers within the explored bias range after current saturation (long time). Note that steady-state current is plotted as a function of the applied electric field $\xi = V/L$, being L the sample thickness, for a better comparison among different structures. The steady-state values in Figure 2 are higher than those encountered with fast cyclic-voltammetry (J - V curve) (Figure S6, Supporting Information). One example is observed in Figure S6b, Supporting Information, with lower electronic current because of a much faster speed of electrons/holes compared to that of ions using a scan rate of 500 mV s^{-1} . That observation signals the necessity of full ion relaxation before concluding about electronic transport regimes in HP devices.^[42]

We express the total characteristic time from the time constant τ of the current transient increase as $t_t = 4\tau$, which relates to the 98% of the transition to the steady state (instead of the 63% when only τ is used). For the sake of simplicity, one can assume a homogeneous ionic charge transport across the device.

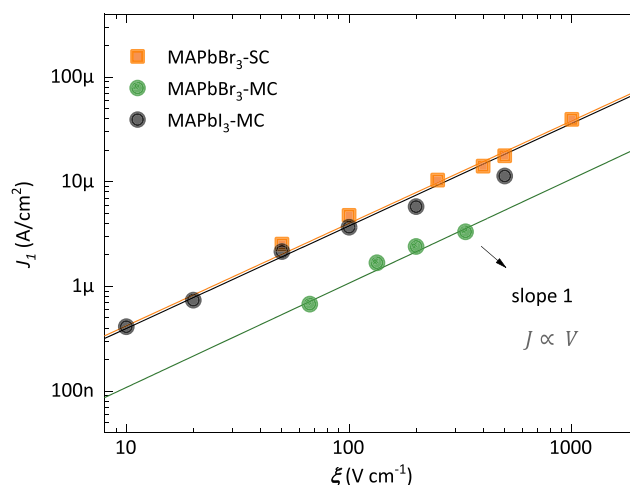


Figure 2. Steady-state current as a function of the electric field ξ during the first current increase step for times $t > 100$ s for three different perovskite samples are shown with the corresponding linear fitting (solid lines). The ohmic behavior is highlighted.

Under these conditions, the ionic time-of-flight mobility μ_i can be estimated through the simple form

$$\mu_i = \frac{L^2}{t_i V} \quad (2)$$

In Figure 3a, the ion mobility has been calculated by using the total time t_i obtained from the first current step (closed dots) for microcrystalline samples of different thicknesses of MAPbI₃. Also plotted in Figure 3a is the μ_i estimated for the second current step (open dots). Remarkably, ionic mobility exhibits a rather constant behavior with the increasing bias independently for the iodide samples.

On the contrary, Figure 3b shows μ_i to increase with the electric field $\xi = V/L$ for MAPbBr₃ with different crystallinity. From the analysis of Figure 3b, using an allometric fitting, one can calculate a power $m \approx 1.2 \pm 0.05$ for the relationship $\mu_i \propto \xi^m$. See below for more comments about this last point.

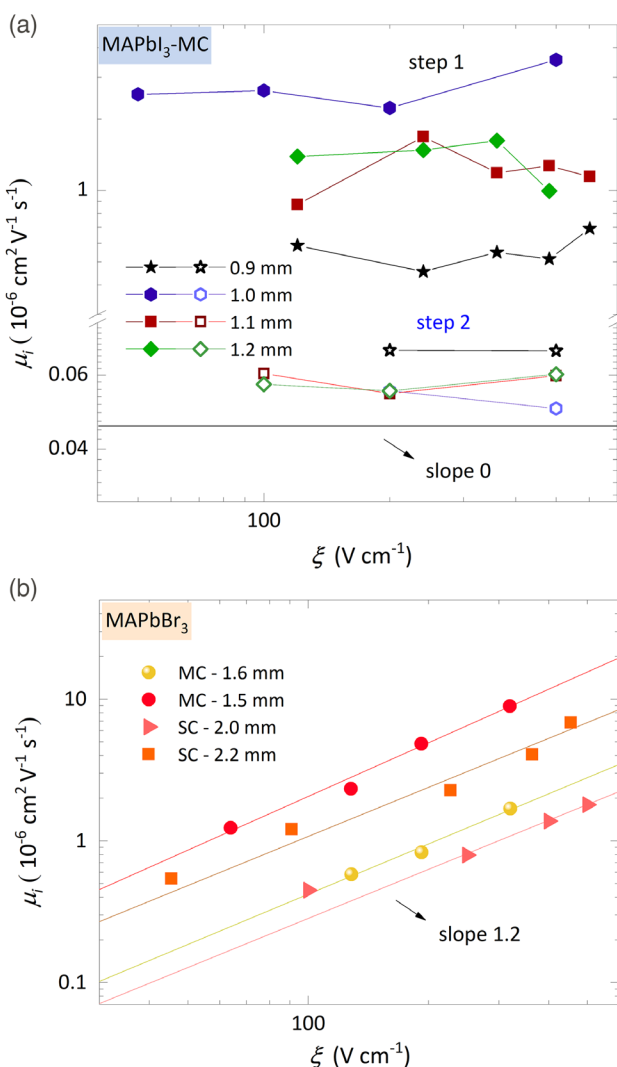


Figure 3. Ion mobility as a function of the electric field ξ for: a) various MAPbI₃-MC perovskite samples and b) two MAPbBr₃-SC and two MC perovskite samples. While a linear trend is clearly observed for bromide compounds, no correlation appears for iodide perovskites.

We also notice that the use of Equation (2) assumes ion drift occurring along the whole sample thickness. Notably, the ion transport would take place in narrow zones $L_{\text{eff}} < L$ (either internal bulk regions or in the vicinity of the external contacts related to the ionic Debye length), meaning that the mobility values represented in Figure 3 could be overestimated.

On mixed conductors as HPs, one must be cautious about whether the measured signals are due to ionic or electronic defects, otherwise mistaken conclusions may be drawn.^[51] Identifying the type of mobile defect is not easy and a number of reports predict the facile migration of halide-related defects, under biasing conditions, rather than MA and Pb vacancies, with calculated activation barriers of ≈ 0.5 and 0.8 eV, respectively.^[6,52] Correlations between specific ionic defects and electronic doping mechanisms have been made based on how the doping concentration is modified during the application and switching-off of an external bias.^[10,48] Recalling now Figure 1, one can speculate about the halide vacancies V_X^+ as the ones that dominate and establish the general time response of the first current step, with typical migration times in the range of 10^{-2} – 10^4 s. Only in the case of MAPbI₃-MC samples (Figure 1c), the second exponential rise can be possibly originated by: 1) imperfections on the perovskite surface or at the grain boundaries introducing alternative, and much slower, ion migration paths; 2) further enhancement in the ion drift of slower migrating defects at higher electric fields, for instance, V_{MA} and V_{Pb} ; or 3) a combination of these effects. Nevertheless, the J_1 values in Figure 2 followed an ohmic regime irrespective of the sample crystallinity or composition, which may indicate that the electronic drift regime is proportional to the electric field in most of the cases. Hence, our findings confirmed that the electronic-ionic coupling mechanism behind the current transients relies on how the ionic movement establishes the kinetics of the electronic carrier response in HPs materials.

Ionic mobility has been determined by many techniques such as impedance spectroscopy (IS),^[48,49,52,53] nuclear magnetic resonance (NMR) spectroscopy,^[54,55] photocurrent transient,^[9,55,56] PL quenching method (PLQ),^[50] temperature-dependent conductivity (TDC) measurement,^[57,58] and chronoamperometry measurements.^[10,49] Previous works shown values between $\mu_i \approx 1$ and $3 \times 10^{-6} \text{ cm}^2 \text{ V}^{-1} \text{ s}^{-1}$ for MAPbBr₃ perovskite SCs by analyzing the resistance response during a diffusion-relaxation mechanism.^[48] The same methodology has been applied for MAPbI₃ thick-pellets^[49] obtaining self-consistent patterns by registering both, current transients and impedance spectra, with values encountered also in the range of $\approx 10^{-6} \text{ cm}^2 \text{ V}^{-1} \text{ s}^{-1}$.

The behavior of μ_i as a function of the electric field in Figure 3a exhibits values within the range of 5×10^{-7} – $3 \times 10^{-6} \text{ cm}^2 \text{ V}^{-1} \text{ s}^{-1}$ for various MC samples of MAPbI₃, which agrees with those reported for the iodine-related defect ionic mobilities. Remarkably, a ξ -independent ion mobility indicates a bulk origin, rather than interfacial, for the mechanism behind the observed electrical response. The μ_i calculated for the second exponential rise is found to be in the order of $\approx 10^{-8} \text{ cm}^2 \text{ V}^{-1} \text{ s}^{-1}$, with a similar, ξ -independent behavior. Therefore, it makes sense to assume, for this second step, that the electronic response relates to other possible moving ions, such as MA⁺ and Pb²⁺ with much lower mobility.^[59,60] This is in accordance with the suppression of MA⁺ migration in MAPbBr₃, while it is actually observed for MAPbI₃.^[61] An alternative explanation for the second step in

the transient response could be related to the role of grain boundaries. However, bromide-based devices, either of single- or MC structure, do not exhibit such a feature at longer times, so as to move us to disregard it as structurally-originated.

By examining Figure 3b, a different trend occurs for bromide samples as $\mu_i \propto \xi^m$, compared to iodine ones. Several models have suggested to rationalize a field-dependent mobility behavior in different materials with $\partial\mu/\partial\xi > 0$. For instance, surface-charge decay in insulators was described to exhibit nonconstant carrier mobility.^[62,63] In the specific case of ion migration in electrolytes of different ionic strength, molecular dynamics simulations recently revealed that ionic conductivity is constant for strong electrolytes. On the contrary, weaker electrolytes or molten salts exhibit applied-field enhancement of the ion mobility.^[64] The field-dependent mobility observed for MAPbBr₃ would indicate a weaker character for the bromide-related defect formation in opposition to a more favorable defect formation of iodide-related ones. Several theoretical predictions for MAPbBr₃ suggest a stronger Pb–Br bond^[65] and considerable lattice contraction by stronger hydrogen bonding to the surrounding Pb–Br₆ octahedra.^[61] These effects could, presumably, increase the bromide-related defect formation energy reducing the observed concentration of bromide mobile ions in MAPbBr₃ compared to iodide concentration in MAPbI₃,^[61] which also explains the superior ambient stability of the bromide compound.

Finally, it is worth mentioning the existence of clear similarities between our findings and the dynamic response of thin-film perovskite devices such as memristors and solar cells. The current increment in the time domain relates to the low-frequency inductive behavior observed in memristors,^[66] and also the change in the conduction regime reported here for MAPbBr₃-MC (initial current reduction followed by current growth) resembles the observation of transient spikes as recently reported.^[67]

3. Conclusions

In summary, long-term dark current has been explored for a set of lead–HP samples of different crystallinity and composition. As a general trend, dark current exhibits an exponential-like rise that reaches steady-state values depending on the applied electrical field. Our findings reveal the coupling between ionic drift and the time scale of the electronic current. MAPbBr₃ and MAPbI₃ exhibit different responses: iodide compounds present double current rise related to the migration of much slower defects such as MA⁺ and Pb²⁺, with much lower values of ion mobility, which are instead suppressed in the case of MAPbBr₃. Also, the dependence of the effective ionic mobility on the electric field presents dissimilar trends: constant, ξ -independent for MAPbI₃, but clearly ξ -dependent in the case of MAPbBr₃. Such a different behavior may be connected to differences in the chemistry of the defect formation between both compounds.

4. Experimental Section

Sample Preparation: Perovskite samples of two compositions, MAPbBr₃ and MAPbI₃, were analyzed. First, SCs of MAPbBr₃ symmetrically contacted with Cr electrodes (see Figure 1a, inset) were prepared following

the inverse temperature crystallization (ITC) growth method previously reported.^[68] MAPbBr₃-SC were grown by the ITC method in *N,N*-dimethylformamide (DMF) anhydrous 99.8%. Here, the perovskite precursors, CH₃NH₃Br and PbBr₂, were dissolved (1:1 mol.%) in DMF to obtain 1 M solutions of MAPbBr₃. All the solutions were stirred at room temperature and filtered using polytetrafluoroethylene filters to remove insoluble particles. An aliquot of the filtered perovskite solutions were placed in a glass flask and the temperature is rise from room to 80–85 °C leading to the spontaneous nucleation and growth of the cubic shape SCs of MAPbBr₃. After mechanically polishing of the single crystal (SC) with sandpaper of different roughness, 100 nm of Cr metal was evaporated at two opposite faces (see Table S1, Supporting Information). An XRD-2D rotation spectrum along the α cell axis was performed to probe the monocrystalline nature of the SC (Figure S7, Supporting Information) and scanning electron microscopy (Figure S9b, Supporting Information) was conducted to observe the smooth surface area of the SC after the polishing process. SC was also characterized by UV–vis spectrophotometry obtaining the corresponding absorption edge for MAPbBr₃ with a bandgap of 2.18 eV (see Tauc plot, Figure S9d, Supporting Information).

Second, MAPbX₃ (X=Br, I) MC pellets of ≈ 1 mm thick asymmetrically contacted with evaporated Pt and Cr electrodes of 1 cm² area (see Figure 1b,c, inset) were made by a soft-sintering process, which is described in detail in ref.[69] The MC pellets with a diameter of ≈ 15 mm were made by a soft-sintering process. The MC MAPbI₃ and MAPbBr₃ powder (Xi'an Polymer Light Technology Corp) were filled into an adjustable height powder container with a polished cylinder placed above it. A constant pressure of 55 MPa (1t) for 30 min at 70 °C results in thick pellets with a thickness of around 1000 μ m. Then, Pt and Cr electrodes were deposited via sputtering and vapor deposition, respectively. MAPbI₃ and MAPbBr₃ MC samples were characterized by UV–vis spectra, scanning electron microscope (SEM) analysis, and X-ray diffraction (XRD) patterns (See Figure S8, Supporting Information). Table S1 in the Supporting Information summarizes the general characteristics of the samples studied. More information about the structural characterization and optoelectronics properties can be found in references^[48,68,70] for MAPbBr₃-SC and^[49,69] for MAPbBr₃-SC samples.

Electrical Measurements: Chronoamperometry measurements were carried out with a Source Measure Unit Model 2612B from Keithley Instruments, Inc. Current measurements were conducted following the long-term DC mode bias protocol in the ranges of ± 200 –0 V as previously reported.^[10] The samples were kept in the dark at ambient temperature and with N₂ circulation to avoid humidity- and oxygen-induced degradations.

Supporting Information

Supporting Information is available from the Wiley Online Library or from the author.

Acknowledgements

This work has received funding from the European Union's Horizon 2020 research and innovation program under the Photonics Public Private Partnership (www.photonics21.org) with the project PEROXIS under the grant agreement N° 871336.

Conflict of Interest

The authors declare no conflict of interest.

Data Availability Statement

The data that support the findings of this study are available from the corresponding author upon reasonable request.

Keywords

dark current, halide-perovskite, ion migration, ion mobility, X-ray detectors

Received: May 9, 2022

Revised: July 26, 2022

Published online: August 17, 2022

- [1] G. R. Monama, K. E. Ramohlola, E. I. Iwuoha, K. D. Modibane, *Results Chem.* **2022**, *4*, 100321.
- [2] H. J. Snaith, *Nat. Mater.* **2018**, *17*, 372.
- [3] O. Almora, P. Lopez-Varo, K. T. Cho, S. Aghazada, W. Meng, Y. Hou, C. Echeverría-Arrondo, I. Zimmermann, G. J. Matt, J. A. Jiménez-Tejada, C. J. Brabec, M. K. Nazeeruddin, G. Garcia-Belmonte, *Sol. Energy Mater. Sol. Cells* **2019**, *195*, 291.
- [4] D. Moia, I. Gelmetti, P. Calado, W. Fisher, M. Stringer, O. Game, Y. Hu, P. Docampo, D. Lidzey, E. Palomares, J. Nelson, P. R. F. Barnes, *Energy Environm. Sci.* **2019**, *12*, 1296.
- [5] J. Bisquert, A. Guerrero, C. Gonzales, *ACS Phys. Chem. Au* **2021**, *1*, 25.
- [6] J. M. Azpiroz, E. Mosconi, J. Bisquert, F. De Angelis, *Energy Environ. Sci.* **2015**, *8*, 2118.
- [7] M. H. Futscher, M. K. Gangishetty, D. N. Congreve, B. Ehrler, *J. Chem. Phys.* **2020**, *152*, 044202.
- [8] D. Shi, V. Adinolfi, R. Comin, M. Yuan, E. Alarousu, A. Buin, Y. Chen, S. Hoogland, A. Rothenberger, K. Katsiev, Y. Losovyj, X. Zhang, P. A. Dowben, O. F. Mohammed, E. H. Sargent, O. M. Bakr, *Science* **2015**, *347*, 519.
- [9] L. Bertoluzzi, C. C. Boyd, N. Rolston, J. Xu, R. Prasanna, B. C. O'Regan, M. D. McGehee, *Joule* **2020**, *4*, 109.
- [10] M. García-Battle, J. Mayén Guillén, M. Chapran, O. Baussens, J. Zaccaro, E. Gros Dailion, J. M. Verilhac, A. Guerrero, O. Almora, G. Garcia Belmonte, *ACS Energy Lett.* **2022**, *7*, 946.
- [11] A. Senocrate, J. Maier, *J. Am. Chem. Soc.* **2019**, *141*, 8382.
- [12] J. Y. Kim, J.-W. Lee, H. S. Jung, H. Shin, N.-G. Park, *Chem. Rev.* **2020**, *120*, 7867.
- [13] H. Dong, H. Yu, X. Wang, Q. Zhou, J. Sun, *J. Chem. Technol. Biotechnol.* **2013**, *88*, 774.
- [14] X. Cheng, E. Fabbri, M. Nachtegaal, I. E. Castelli, M. El Kazzi, R. Haumont, N. Marzari, T. J. Schmidt, *Chem. Mater.* **2015**, *27*, 7662.
- [15] A. Colmann, H. Röhm, *J. Phys.: Energy* **2019**, *2*, 011003.
- [16] L. Fu, B. Li, S. Li, L. Yin, in *Revolution of Perovskite: Synthesis, Properties and Applications* (Eds: N. S. Arul, V. D. Nithya), Springer Singapore, Singapore **2020**, p. 43.
- [17] L. Yang, Y. Li, Y. Sun, W. Wang, Z. Shao, *Energy Environ. Mater.* **2021**, *1*.
- [18] Q. A. Akkerman, L. Manna, *ACS Energy Lett.* **2020**, *5*, 604.
- [19] L. Zhu, R. Ran, M. Tadó, W. Wang, Z. Shao, *Asia-Pac. J. Chem. Eng.* **2016**, *11*, 338.
- [20] W. W. Wolszczak, D. L. Carroll, R. T. Williams, in *Advanced X-ray Detector Technologies: Design and Applications* (Ed: K. Iniewski), Springer International Publishing, Cham **2022**, p. 1.
- [21] R. Tan, B. Dryzhakov, J. Charest, B. Hu, M. Ahmadi, E. Lukosi, *Nucl. Instrum. Methods Phys. Res., Sect. A* **2021**, *986*, 164710.
- [22] Y. He, L. Matei, H. J. Jung, K. M. McCall, M. Chen, C. C. Stoumpos, Z. Liu, J. A. Peters, D. Y. Chung, B. W. Wessels, M. R. Wasielewski, V. P. Dravid, A. Burger, M. G. Kanatzidis, *Nat. Commun.* **2018**, *9*, 1609.
- [23] H. Tsai, J. Tisdale, S. Shrestha, F. Liu, W. Nie, in *Advanced X-ray Detector Technologies: Design and Applications* (Ed: K. Iniewski), Springer International Publishing, Cham **2022**, p. 35.
- [24] H. Wei, J. Huang, *Nat. Commun.* **2019**, *10*, 1066.
- [25] H. Wei, Y. Fang, P. Mulligan, W. Chuirazzi, H. H. Fang, C. Wang, B. R. Ecker, Y. Gao, M. A. Loi, L. Cao, J. Huang, *Nat. Photonics* **2016**, *10*, 333.
- [26] M. I. Saidaminov, A. L. Abdelhady, B. Murali, E. Alarousu, V. M. Burlakov, W. Peng, I. Dursun, L. Wang, Y. He, G. Maculan, A. Goriely, T. Wu, O. F. Mohammed, O. M. Bakr, *Nat. Commun.* **2015**, *6*, 7586.
- [27] F. Liu, R. Wu, J. Wei, W. Nie, A. D. Mohite, S. Brovelli, L. Manna, H. Li, *ACS Energy Lett.* **2022**, *7*, 1066.
- [28] J.-X. Wang, L. Gutiérrez-Arzaluz, X. Wang, M. Almalki, J. Yin, J. Czaban-Jóźwiak, O. Shekhah, Y. Zhang, O. M. Bakr, M. Eddaoudi, O. F. Mohammed, *Matter* **2022**, *5*, 253.
- [29] J. A. Rowlands, D. M. Hunter, N. Araj, *Med. Phys.* **1991**, *18*, 421.
- [30] S. O. Kasap, *J. Phys. D: Appl. Phys.* **2000**, *33*, 2853.
- [31] Y. Liu, Z. Xu, Z. Yang, Y. Zhang, J. Cui, Y. He, H. Ye, K. Zhao, H. Sun, R. Lu, M. Liu, M. G. Kanatzidis, S. Liu, *Matter* **2020**, *3*, 180.
- [32] R. Zhuang, X. Wang, W. Ma, Y. Wu, X. Chen, L. Tang, H. Zhu, J. Liu, L. Wu, W. Zhou, X. Liu, Y. Yang, *Nat. Photonics* **2019**, *13*, 602.
- [33] X. Zheng, W. Zhao, P. Wang, H. Tan, M. I. Saidaminov, S. Tie, L. Chen, Y. Peng, J. Long, W.-H. Zhang, *J. Energy Chem.* **2020**, *49*, 299.
- [34] Y. Song, L. Li, M. Hao, W. Bi, A. Wang, Y. Kang, H. Li, X. Li, Y. Fang, D. Yang, Q. Dong, *Adv. Mater.* **2021**, *33*, 2103078.
- [35] T. Zhou, T. Zhang, *Small Methods* **2021**, *5*, 2100515.
- [36] M. Karmaoui, S. G. Leonardi, M. Latino, D. M. Tobaldi, N. Donato, R. C. Pullar, M. P. Seabra, J. A. Labrincha, G. Neri, *Sens. Actuators, B* **2016**, *230*, 697.
- [37] D. Zhou, D. Liu, G. Pan, X. Chen, D. Li, W. Xu, X. Bai, H. Song, *Adv. Mater.* **2017**, *29*, 1704149.
- [38] R. Sun, P. Lu, D. Zhou, W. Xu, N. Ding, H. Shao, Y. Zhang, D. Li, N. Wang, X. Zhuang, B. Dong, X. Bai, H. Song, *ACS Energy Lett.* **2020**, *5*, 2131.
- [39] C. Wang, B. R. Ecker, H. Wei, J. Huang, Y. Gao, *J. Phys. Chem. C* **2018**, *122*, 3513.
- [40] Y. Song, L. Li, W. Bi, M. Hao, Y. Kang, A. Wang, Z. Wang, H. Li, X. Li, Y. Fang, D. Yang, Q. Dong, *Research* **2020**, *2020*, 5958243.
- [41] Z. Pan, L. Wu, J. Jiang, L. Shen, K. Yao, *J. Phys. Chem. Lett.* **2022**, *13*, 2851.
- [42] E. A. Duijnste, V. M. Le Corre, M. B. Johnston, L. J. A. Koster, J. Lim, H. J. Snaith, *Phys. Rev. Appl.* **2021**, *15*, 014006.
- [43] B. Murali, H. K. Kolli, J. Yin, R. Ketavath, O. M. Bakr, O. F. Mohammed, *ACS Mater. Lett.* **2020**, *2*, 184.
- [44] D. Li, H. Wu, H.-C. Cheng, G. Wang, Y. Huang, X. Duan, *ACS Nano* **2016**, *10*, 6933.
- [45] O. Almora, C. Aranda, I. Zarazua, A. Guerrero, G. Garcia-Belmonte, *ACS Energy Lett.* **2016**, *1*, 209.
- [46] G. Garcia-Belmonte, J. Bisquert, *ACS Energy Letters* **2016**, *1*, 683.
- [47] J. Bisquert, A. Guerrero, *J. Am. Chem. Soc.* **2022**, *144*, 5996.
- [48] M. García-Battle, O. Baussens, S. Amari, J. Zaccaro, E. Gros-Dailion, J. M. Verilhac, A. Guerrero, G. Garcia-Belmonte, *Adv. Electron. Mater.* **2020**, *6*, 2000485.
- [49] M. García-Battle, S. Deumel, J. E. Huerdler, S. F. Tedde, A. Guerrero, O. Almora, G. Garcia-Belmonte, *ACS Appl. Mater. Interfaces* **2021**, *13*, 35617.
- [50] C. Li, A. Guerrero, S. Huettner, J. Bisquert, *Nat. Commun.* **2018**, *9*, 5113.
- [51] M. H. Futscher, C. Deibel, *ACS Energy Lett.* **2022**, *7*, 140.
- [52] W. Peng, C. Aranda, O. M. Bakr, G. Garcia-Belmonte, J. Bisquert, A. Guerrero, *ACS Energy Lett.* **2018**, *3*, 1477.
- [53] S.-G. Kim, C. Li, A. Guerrero, J.-M. Yang, Y. Zhong, J. Bisquert, S. Huettner, N.-G. Park, *J. Mater. Chem. A* **2019**, *7*, 18807.
- [54] A. Senocrate, I. L. Moudrakovski, G. Y. Kim, T.-Y. Yang, G. Gregori, M. Grätzel, J. Maier, *Angew. Chem., Int. Ed.* **2017**, *56*, 7755.
- [55] A. Senocrate, I. L. Moudrakovski, T. Acartürk, R. Merkle, G. Y. Kim, U. Starke, M. Grätzel, J. Maier, *J. Phys. Chem. C* **2018**, *122*, 21803.

- [56] R. A. Belisle, W. H. Nguyen, A. R. Bowring, P. Calado, X. Li, S. J. C. Irvine, M. D. McGehee, P. R. F. Barnes, B. C. O'Regan, *Energy Environ. Sci.* **2017**, *10*, 192.
- [57] Y. Lin, B. Chen, Y. Fang, J. Zhao, C. Bao, Z. Yu, Y. Deng, P. N. Rudd, Y. Yan, Y. Yuan, J. Huang, *Nat. Commun.* **2018**, *9*, 4981.
- [58] Y. Yuan, J. Chae, Y. Shao, Q. Wang, Z. Xiao, A. Centrone, J. Huang, *Adv. Energy Mater.* **2015**, *5*, 1500615.
- [59] T.-Y. Yang, G. Gregori, N. Pellet, M. Grätzel, J. Maier, *Angew. Chem., Int. Ed.* **2015**, *54*, 7905.
- [60] S. A. L. Weber, I. M. Hermes, S.-H. Turren-Cruz, C. Gort, V. W. Bergmann, L. Gilson, A. Hagfeldt, M. Graetzel, W. Tress, R. Berger, *Energy Environ. Sci.* **2018**, *11*, 2404.
- [61] L. McGovern, M. H. Futscher, L. A. Muscarella, B. Ehrler, *J. Phys. Chem. Lett.* **2020**, *11*, 7127.
- [62] H. J. Wintle, *J. Appl. Phys.* **1972**, *43*, 2927.
- [63] T. J. Sonnonstine, M. M. Perlman, *J. Appl. Phys.* **1975**, *46*, 3975.
- [64] D. Lesnicki, C. Y. Gao, B. Rotenberg, D. T. Limmer, *Phys. Rev. Lett.* **2020**, *124*, 206001.
- [65] S. J. Yoon, K. G. Stamplecoskie, P. V. Kamat, *J. Phys. Chem. Lett.* **2016**, *7*, 1368.
- [66] L. Munoz-Diaz, A. J. Rosa, A. Bou, R. S. Sánchez, B. Romero, R. A. John, M. V. Kovalenko, A. Guerrero, J. Bisquert, *Front. Energy Res.* **2022**, *10*, 914115.
- [67] E. Hernández-Balaguera, J. Bisquert, *ACS Energy Lett.* **2022**, *7*, 2602.
- [68] S. Amari, J.-M. Verilhac, E. Gros D'Aillon, A. Ibanez, J. Zaccaro, *Cryst. Growth Des.* **2020**, *20*, 1665.
- [69] S. Deumel, A. van Breemen, G. Gelinck, B. Peeters, J. Maas, R. Verbeek, S. Shanmugam, H. Akkerman, E. Meulenkaamp, J. E. Huedler, M. Acharya, M. García-Battle, O. Almora, A. Guerrero, G. Garcia-Belmonte, W. Heiss, O. Schmidt, S. F. Tedde, *Nat. Electron.* **2021**, *4*, 681.
- [70] O. Baussens, L. Maturana, S. Amari, J. Zaccaro, J.-M. Verilhac, L. Hirsch, E. Gros-Daillon, *Appl. Phys. Lett.* **2020**, *117*, 041904.